Atmospheric Environment 106 (2015) 262–277

Contents lists available at ScienceDirect

Atmospheric Environment

journal homepage: www.elsevier.com/locate/atmosenv

Satellite observations of tropospheric ammonia and carbon monoxide: Global distributions, regional correlations and comparisons to model simulations

Ming Luo [a, *], Mark W. Shephard [b], Karen E. Cady-Pereira [c], Daven K. Henze [d], Liye Zhu [d], Jesse O. Bash [e], Robert W. Pinder [e], Shannon L. Capps [e], John T. Walker [e], Matthew R. Jones [e, f]

[a] Jet Propulsion Laboratory, California Institute of Technology, Pasadena, CA 91109, USA
[b] Environment Canada, Toronto, Ontario, Canada
[c] Atmospheric and Environmental Research, Inc., Lexington, MA, USA
[d] University of Colorado, Boulder, CO, USA
[e] US Environmental Protection Agency, Research Triangle Park, NC, USA
[f] Center for Ecology and Hydrology, Edinburgh, Penicuik, UK

HIGHLIGHTS

- TES satellite observations of global distributions and correlations of NH_3 and CO.
- GEOS-Chem model simulations of NH_3 and CO are used in investigations.
- In biomass burning regions the NH_3:CO ratios are 0.015 (TES) and 0.013 (GEOS-Chem).
- In regions with mixed anthropogenic sources, NH_3:CO ratios are 0.051 (TES) and 0.036 (GEOS-Chem).

ARTICLE INFO

Article history:
Received 2 July 2014
Received in revised form
28 January 2015
Accepted 4 February 2015
Available online 7 February 2015

Keywords:
Satellite observations of carbon monoxide and ammonia
GEOS-Chem model simulations

ABSTRACT

Ammonia (NH_3) and carbon monoxide (CO) are primary pollutants emitted to the Earth's atmosphere from common as well as distinct sources associated with anthropogenic and natural activities. The seasonal and global distributions and correlations of NH_3 and CO from the Tropospheric Emission Spectrometer (TES) satellite observations and GEOS-Chem model simulations for 2007 are investigated to evaluate how well the global and seasonal pollutant sources are prescribed in the model. Although the GEOS-Chem simulations of NH_3 and CO atmospheric mixing ratio values are lower than the TES satellite observations, the global distribution patterns from the model reasonably agree with the observations, indicating that the model represents the general location of the source regions and the seasonal enhancements of NH_3 and CO globally over large regional scales. In regions and seasons where biomass burning is the dominant source of both NH_3 and CO emissions into the atmosphere, there are strong NH_3:CO correlations, which is consistent with the relationship demonstrated by surface measurements over fires. In regions where the enhanced NH_3 and CO are known to be produced by different sources, the NH_3:CO correlations from TES observations and model simulations are weak or non-existent. For biomass burning regions the NH_3:CO ratios are 0.015 (TES) and 0.013 (GEOS-Chem). In regions of high-population density, known heavy traffic, and limited biomass burning sources, such as the rapidly developing areas of South Asia and northern China, which include mixtures of megacities, industrial, and agricultural areas, the two species show weaker but still positive correlations and NH_3:CO ratios of 0.051 (TES) and 0.036 (GEOS-Chem). These enhancement ratios of NH_3 relative to CO are useful in constraining NH_3 emission inventories when CO emission inventories are better known for some events or regions (i.e. biomass burning).

* Corresponding author.
E-mail address: Ming.Luo@jpl.nasa.gov (M. Luo).

http://dx.doi.org/10.1016/j.atmosenv.2015.02.007
1352-2310/

1. Introduction

Carbon monoxide (CO) is a colorless and toxic gas with both direct (Raub et al., 2000) and indirect (White et al., 1989) impacts on human health and the environment. CO can be oxidized to form carbon dioxide (CO_2) – an important greenhouse gas. It is also a precursor of ozone (O_3) under high NO_x conditions. Although ammonia (NH_3) is short-lived (hours to days) it also plays an important role in the atmosphere, as it reacts with sulfuric acid and nitric acid to form ammonium sulfate and ammonium nitrate aerosols, which can be transported over greater distances (~100 km) then ammonia in the gas-phase; these aerosols are constituents of fine particulate matter ($PM_{2.5}$), which harms human health (e.g., Crouse et al., 2012) and impacts climate by changing the number of cloud condensation nuclei (CCN) and thus affecting cloud radiative properties (e.g., Forster et al., 2007; Langridge et al., 2012). The lifetime of CO (weeks to months) makes it an important transported pollutant that can have intercontinental-scale impacts (Liang et al., 2004; Yashiro et al., 2009). NH_3 emissions are mainly from agricultural practices, e.g., livestock waste management and fertilizer application (Beusen et al., 2008), while CO and NH_3 both have emissions sources from biomass burning (i.e. wildfires, agriculture fires, and prescribed land management burning), and fossil fuel combustion (Akagi et al., 2011). The other source for CO production is the oxidation of methane and non-methane hydrocarbons (NMHCs). Large uncertainties exist in both CO and NH_3 bottom-up emission inventories (e.g., Zhao et al., 2011; Pinder et al., 2006). These affect the performances of model simulations of the distribution of the atmospheric constituents.

Instruments on earth-orbiting satellites launched in the last 10 years provide estimates of atmospheric pollutant amounts in the troposphere based on high spectral resolution radiance measurements. These observations provide global distributions of key species for studies of atmospheric processes and to constrain emission inventories in model simulations. The sources and distributions of NH_3 and CO, as well as their roles in atmospheric chemistry respectively, have been studied in different regions using satellite and in-situ and model simulations (e.g. Edwards et al., 2004; Edwards et al., 2006; Luo et al., 2007a; Clarisse et al., 2009; Shephard et al., 2011; Boynard et al., 2013; Van Damme et al., 2014). In this paper we examine the relationships and distributions of CO and NH_3 globally from the Tropospheric Emission Spectrometer (TES) flying on board the NASA AURA satellite (Beer, 2006). Calculating the observed NH_3:CO correlations (emission ratios) for the pollutants and comparing them to the model simulations provides valuable insight on trace gas emission sources, and can be used to evaluate the performance of the chemistry transport model globally. Satellite observations of NH_3 enhancement ratio relative to CO in the fire regions can also be compared to recent enhancement ratios derived from in-situ measurements (Akagi et al., 2011), and ground-based remotely sensed values (Paton-Walsh et al., 2014; Smith et al., 2014). The known NH_3 and CO ratio in regions of their common combustion sources is useful in determining NH_3 emissions from the better known CO emissions (Hegg et al., 1988). Their established relationships under different conditions are also useful in regions where the air is influenced by the transport from remote sources.

We examine TES data and the GEOS-Chem model simulations of CO and NH_3 globally for 2007. In Section 2 we describe TES tropospheric observations of global CO and NH_3, the GEOS-Chem simulations, and the representative volume mixing ratios (RVMRs) comparison methodology. In Section 3, we present and compare the CO and NH_3 global distributions from TES and GEOS-Chem. In Section 4 we examine the correlations between the two species from GEOS-Chem simulations with and without biomass burning sources, and TES observations. We summarize the conclusions in Section 5.

2. TES observations and GEOS-Chem data

2.1. TES instrument and data

The TES instrument on the Aura satellite is a nadir-viewing high spectral resolution (0.1 cm^{-1}; apodized) infrared Fourier Transform spectrometer (FTS) (Beer, 2006). TES's high spectral resolution, low radiometric noise (Shephard et al., 2008) and good stability (Connor et al., 2011) enable it to measure a suite of coincident and co-located tropospheric species used for air quality studies, including NH_3 and CO. TES uses a spectral feature around 967 cm^{-1} in the ν_2 vibrational band centered around 950 cm^{-1} to measure NH_3 (Shephard et al., 2011). NH_3 profiles with a minimum peak profile value of ~1 ppbv are usually detectable by TES (Shephard et al., 2011). TES has ~1:30 am and 1:30 pm Equator crossing times. The early afternoon crossing provides good thermal contrast between the surface and the lower atmosphere allowing for increased detectability of NH_3 (Clarisse et al., 2010). The TES NH_3 retrievals are mainly sensitive to NH_3 in the lower troposphere between 700 and 900 hPa, with degrees of freedom for signal (DOFS) typically less than 1 DOFS (Shephard et al., 2011). TES NH_3 has shown good correlation with *in situ* measurements taken in N Carolina, 2009 (Pinder et al., 2011) and California, 2010 (Cady-Pereira et al., 2013).

TES CO profiles are retrieved from the strong absorption (1–0) band at 4.6 μm. The CO retrieved profiles are broadly sensitive to the lower-mid troposphere with DOFS of 0.5–2 in the tropics and mid-latitudes with 10–20% retrieval errors (Rinsland et al., 2006; Luo et al., 2007a). TES CO profiles have been extensively validated against aircraft measurements and the MOPITT (Measurements of Pollution in the Troposphere) satellite data (Luo et al., 2007a,b; Lopez et al., 2008; Ho et al., 2009). Although TES CO is slightly lower than comparable measurements by less than a few percent, the global distributions agree well with other satellite observations (Luo et al., 2007a; George et al., 2009; Worden et al., 2013).

The TES CO and NH_3 data presented in this paper are obtained from the version V005 data products (http://avdc.gsfc.nasa.gov/index.php?site=635564035&id=10). Data from both Global Surveys (GS) and Special Observation (SO) modes were included in this analysis. TES GSs consist of 16 orbits every other day, while the SOs operations are carried out on the GS 'off' days. The SOs are scheduled during science and validation campaigns in regional transect, step-and-stare, or stare modes (Beer, 2006).

In this analysis, both TES and model data are grouped into four seasons: Jan–Feb and Dec 2007, March–May 2007, June–Aug 2007, and Sept–Nov 2007. The TES observations in 2007 were selected for the analysis as the largest CO enhancements in the tropical biomass burning regions are observed during this year.

2.2. TES retrievals

The TES operational retrieval model is an optimal estimation approach that minimizes the difference between the observed spectral radiances and the radiances calculated from a nonlinear radiative transfer model driven by the atmospheric state, subject to the constraint that the estimated state must be consistent with an *a priori* probability distribution for that state (Rodgers, 2000; Bowman et al., 2006; Shephard et al., 2011). One of the benefits of the optimal estimation retrieval approach is that both the sensitivity of the retrieval to the true atmospheric state (averaging kernels), and estimates of the retrieval errors (error covariance) are direct products of the retrieval and are available for in-depth

analysis of the satellite observations. To compute the forward model radiances the TES fast forward model is used; the model's absorption coefficients are generated by the well-validated Line-By-Line Radiative Transfer Model (LBLRTM) (Clough et al., 2006; Shephard et al., 2008; Alvarado et al., 2013).

2.3. Representative tropospheric VMR for NH_3 and CO

Even though there is limited information available from minor trace gas species retrievals (Degree of Freedom for Signal is less than 2), the retrieval sensitivity still varies from profile-to-profile depending on the atmospheric state. To capture this sensitivity, the retrievals are performed at more levels than there is available information for. Therefore, at any given single profile level the retrieved NH_3 VMR is substantially influenced by the *a priori* profile. To address this issue for different purposes (i.e. for 2-D maps or comparison with surface data) we computed representative volume mixing ratio values (RVMR) (Shephard et al., 2011). The RVMR is a "weighted" average over the vertical portion of the profile where TES is sensitive, which reduces the influence of the *a priori* as much as possible. The level to which the influence is reduced depends on the available retrieval information content for the observation: if there is one piece of information from a given retrieval then a single RVMR value can be generated with almost all of the *a priori* removed, making comparison with *in situ* measurements simpler. The RVMR pressure is defined as the center of this vertical extent. The RVMR is computed directly from the vertical sensitivity of TES retrieval using a transformation matrix, $\boldsymbol{W_{i,j}}$, that maps the retrieved NH_3 VMR values from all the retrieval levels, i, onto a subset of RVMR levels, j, which is more representative of the information provided by the measurement, as compared to just selecting a single retrieval level. Note that $\boldsymbol{W_{i,j}}$ is in log space, as are the retrievals, and thus the averaging kernels on which $\boldsymbol{W_{i,j}}$ is based. The RVMR (ρ) is computed as follows (Shephard et al., 2011; Wells et al., 2014):

$$\rho_j = e^{\left[\sum_{i=1}^{nlevs} log(\widehat{x}_i)\, \boldsymbol{W_{i,j}}\right]} \quad (1)$$

For retrievals with limited amount of information (i.e. DOFS < 1.0), there is often only one RVMR value produced ($j = 1$): the $\boldsymbol{W_{i,j}}$, matrix is reduced to a vector W_i, and Equation (1) simplifies to:

$$\rho_1 = e^{\left[\sum_{i=1}^{n_{levs}} log(\widehat{x}_i)\, W_i\right]} \quad (2)$$

TES NH_3 and CO retrievals are first quality screened as described in the TES Level 2 Data User's Guide (Herman and Kulawik, 2013). Additional screening for NH_3 is used following section 6.2.1.3 "Additional guide for NH_3 data quality" in the User's Guide. These include only retrievals with at least 0.1 degrees-of-freedom-for-signal (DOFS), under conditions with cloud optical depths <2.0, and surface temperatures >278 K. For DOFS between 0.1 and 0.5, special instructions are provided. For this study, an additional quality control was also performed by visually examining the Level 1B NH_3 spectra for retrievals with very large elevated NH_3 values to make sure the retrieval had returned a reasonable result. Since the peak retrieval sensitivity pressure for NH_3 is usually within the broader vertical sensitivity of CO, the retrieved CO VMRs are mapped onto the corresponding NH_3 VMR pressures and the "weighing functions" for calculating NH_3 RVMRs are applied to CO profiles to obtain the CO RVMRs. This is similar to the approach taken for the TES CH_3OH:CO relationship comparison performed by Wells et al. (2014). These pseudo CO RVMRs computed using the NH_3 RVMR mapping are reported in this paper instead of CO VMRs to facilitate direct comparison of the NH_3:CO relationships over the same altitude range.

2.4. GEOS-Chem

The GEOS-Chem chemical transport model is driven by assimilated meteorology from the Goddard Earth Observing System (GEOS) of the NASA Global Modeling and Assimilation Office. We use GEOS-Chem version v8-02-01 with a horizontal resolution $2^\circ \times 2.5^\circ$. GEOS-Chem includes a detailed ozone-NO_x-hydrocarbon-aerosol chemical mechanism coupled with sulfate-nitrate-ammonia aerosol thermodynamics (Park et al., 2004). The partition of secondary inorganic species between gas and aerosol phase is estimated with RPMARES thermodynamic equilibrium model (Binkowski and Roselle, 2003). The wet deposition scheme of soluble aerosols and gases is based on Liu et al. (2001). The dry deposition of aerosols and gases scheme is based on the resistance-in-series model described in Wesely (1989).

The global anthropogenic sources of CO are from the Emissions Database for Global Atmospheric Research (EDGAR) inventory (Olivier and Berdowski, 2001), updated by the regional emission inventories: The US Environmental Protection Agency National Emission Inventory for 2005 in North America (ftp://aftp.fsl.noaa.gov/divisions/taq/emissions_data_2005/Weekday_emissions/readme.txt), the Criteria Air Contaminants (CAC) inventory for Canada (http://www.ec.gc.ca/pdb/cac/cac_home_e.cfm), the inventory of Streets et al. (2006) for Asia, the Big Bend Regional Aerosol and Visibility Observational (BRAVO) Study emissions inventory for Mexico (Kuhns et al., 2005), and the Co-operative Program for Monitoring and Evaluation of the Long-range Transmission of Air Pollutants in Europe (EMEP) inventory for Europe (Vestreng and Klein, 2002). The global anthropogenic sources and natural sources of NH_3 are from the 1990 GEIA inventory (Bouwman et al., 1997) and updated by the regional emission inventories: Park et al. (2004) over the U.S., the CAC inventory for Canada (van Donkelaar et al., 2008), and the EMEP inventory for Europe. Biomass burning emissions of CO and NH_3 are from the GFED2 inventory with monthly resolution (van der Werf et al., 2006). Biofuel emissions of NH_3 are from Yevich and Logan (2003). The daily average profiles of NH_3 and CO for 2007 are simulated with and without biomass burning emissions.

2.5. Comparison methodology

The GEOS-Chem model fields of NH_3 and CO are spatially and temporally sampled at TES measurement locations and times. For comparison purposes an estimated model profile, $\boldsymbol{x}^{est}{}_{model}$, representing what TES would measure for the same air mass sampled by the model was computed following the standard procedures for performing comparisons between the model species simulation and the satellite retrievals (e.g., TES Level 2 Data User's Guide, 2013). The merit of this comparison approach is that it accounts for the retrieval a-priori bias and the sensitivity (i.e. vertical resolution) of the satellite retrievals. This is accomplished by applying the TES averaging kernel, $\boldsymbol{A}$, and the a-priori profile, x_a, to the model profiles that have been mapped onto the retrieval grid levels, x_{model}^{mapped},

$$x_{model}^{est} = x_a + \boldsymbol{A}\left(x_{model}^{mapped} - x_a\right) \quad (3)$$

Note that differences between x_{model}^{est} and the satellite retrieved parameter $\widehat{x}$ go to zero in regions where the TES retrieval contains little information from the measurement ($\boldsymbol{A} \rightarrow 0$) and the retrieval effectively returns the a-priori. In this study, these situations are avoided by selecting TES observations with adequate information

using criterion recommended in TES Date User's Guide section 6.2.1.3 (Herman and Kulawik, 2013). Finally, the generated x_{model}^{est} are used to compute the GEOS-Chem RVMRs for NH_3 and CO. Fig. 1 shows examples of the above described profiles and RVMRs. The corresponding TES averaging kernels are also shown. In these cases, TES measurements have adequate sensitivity, as shown in the AK, which allows the estimated model profiles to stay close to the original model profile in the lower troposphere, as they are not strongly influenced by the *a priori* profile. In the mid-upper troposphere, the estimated model profiles more closely follow the *a priori*. The "double peak" shape in the original model CO profile is not resolvable by the TES observation. This is reflected in the shape of the estimated model CO profile with a shape that follows the *a priori*. However, the computed model CO RVMR reasonably represents the CO VMR in the lower troposphere.

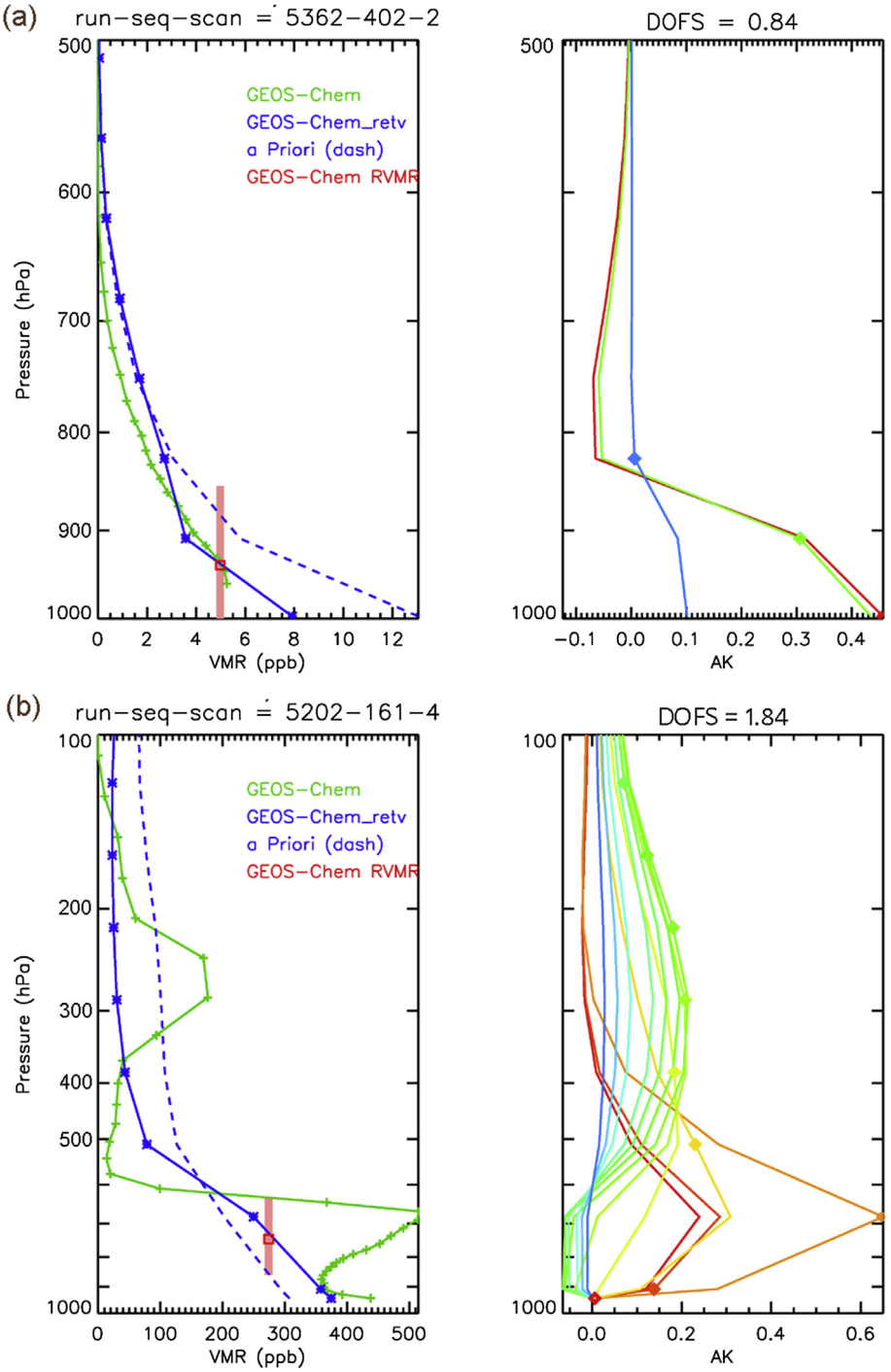

Fig. 1. Examples of species profiles (left panels) and TES averaging kernels (right panels) for NH_3 (a) and for CO (b). The left panels illustrate the *a priori* profile, the GEOS-Chem original profile, and the adjusted GEOS-Chem profile with TES retrieval operator applied ($\boldsymbol{x}_{\boldsymbol{model}}^{\boldsymbol{est}}$) and the corresponding GEOS-Chem RVMR. The right panels show the rows of the averaging kernels.

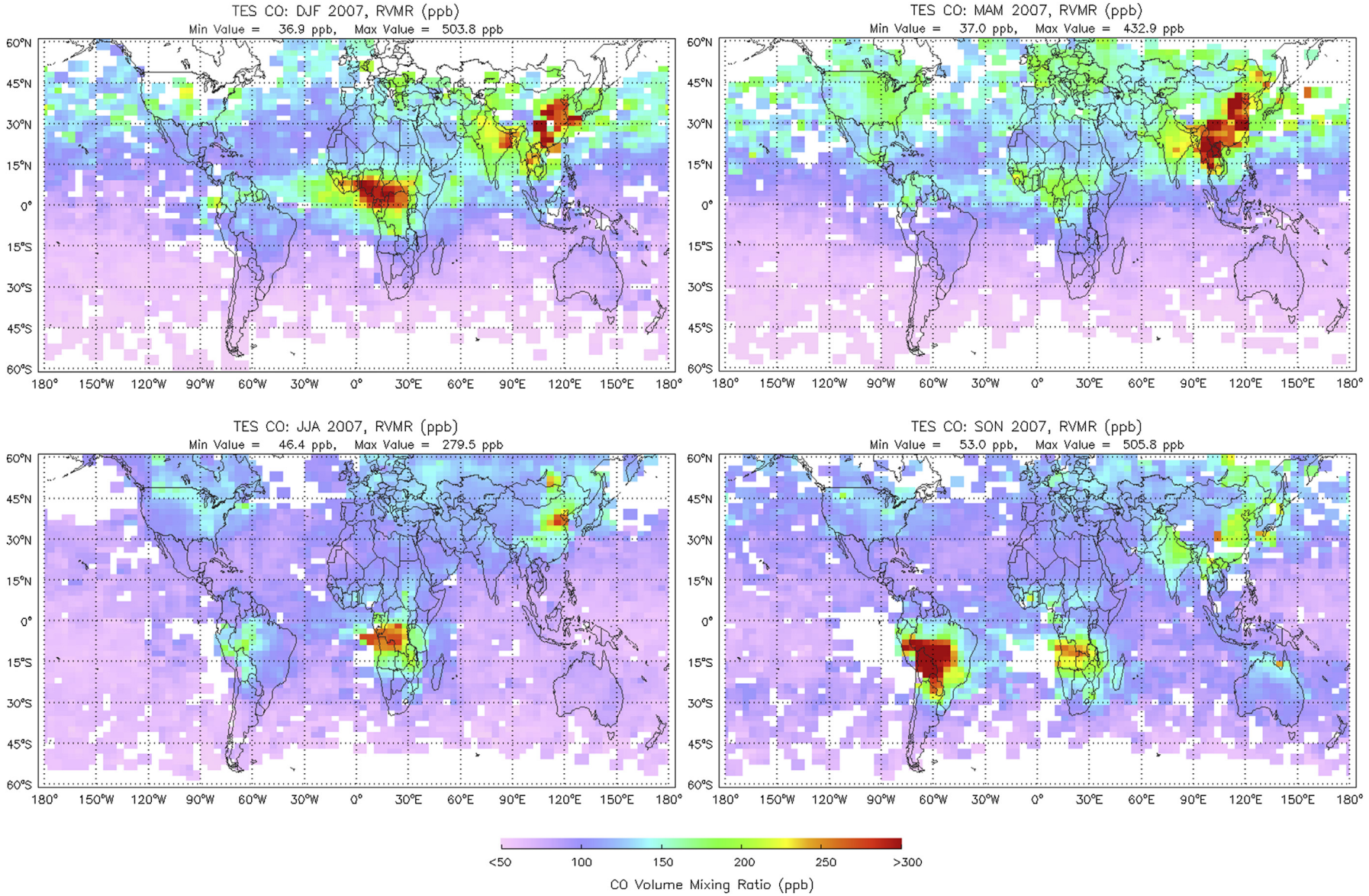

Fig. 2. Global averages of TES CO RVMR for four seasons in 2007. Data are averaged over 2° latitude by 4° longitude bins inversely weighted by the error in RVMR and distance to the center of the bin boxes.

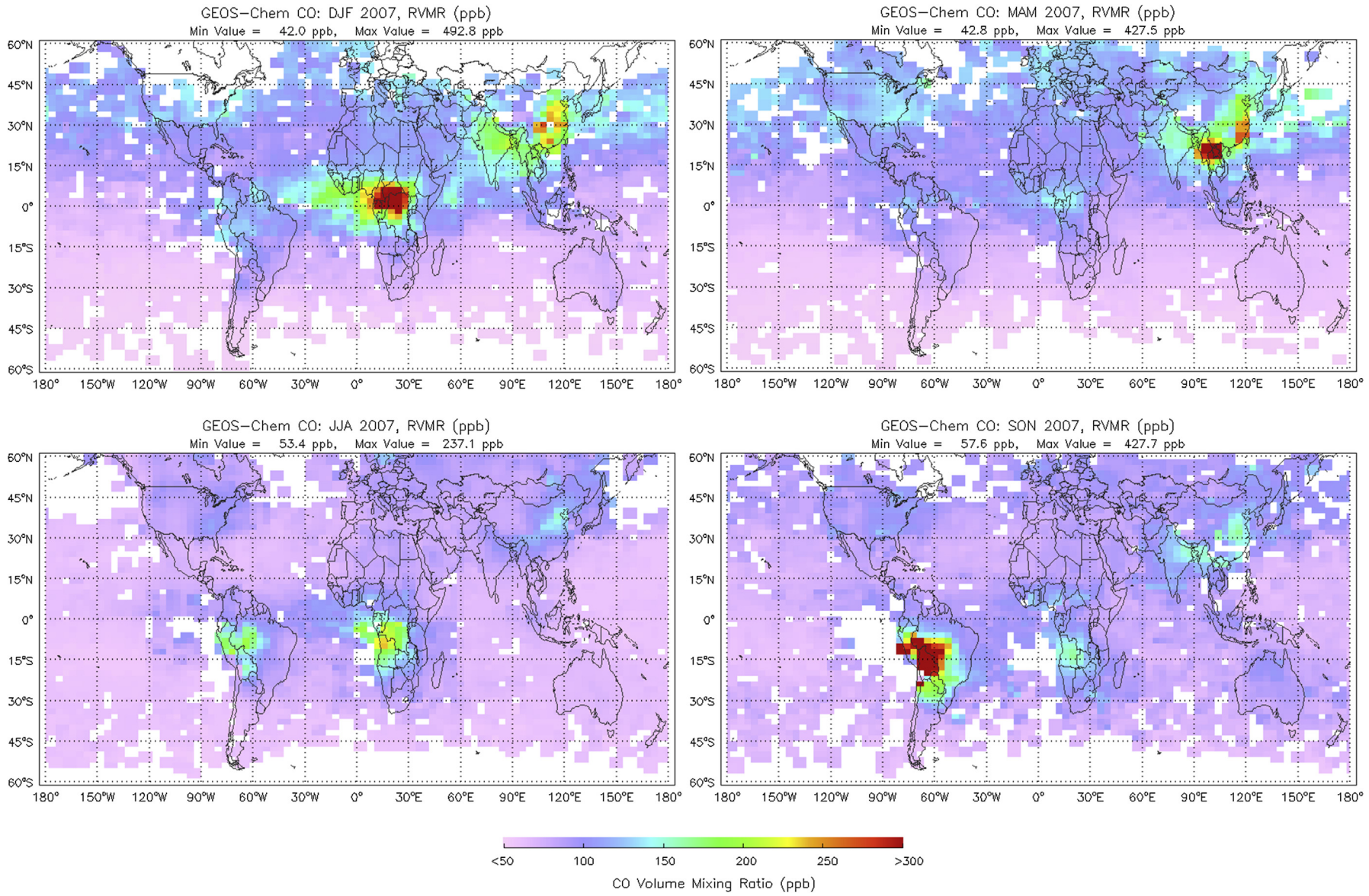

Fig. 3. Global averages of GEOS-Chem CO RVMR for four seasons in 2007. Model data are sampled at TES observation locations and times; CO RVMR is calculated after the TES observation operator is applied; data are averaged over 2° latitude by 4° longitude bins.

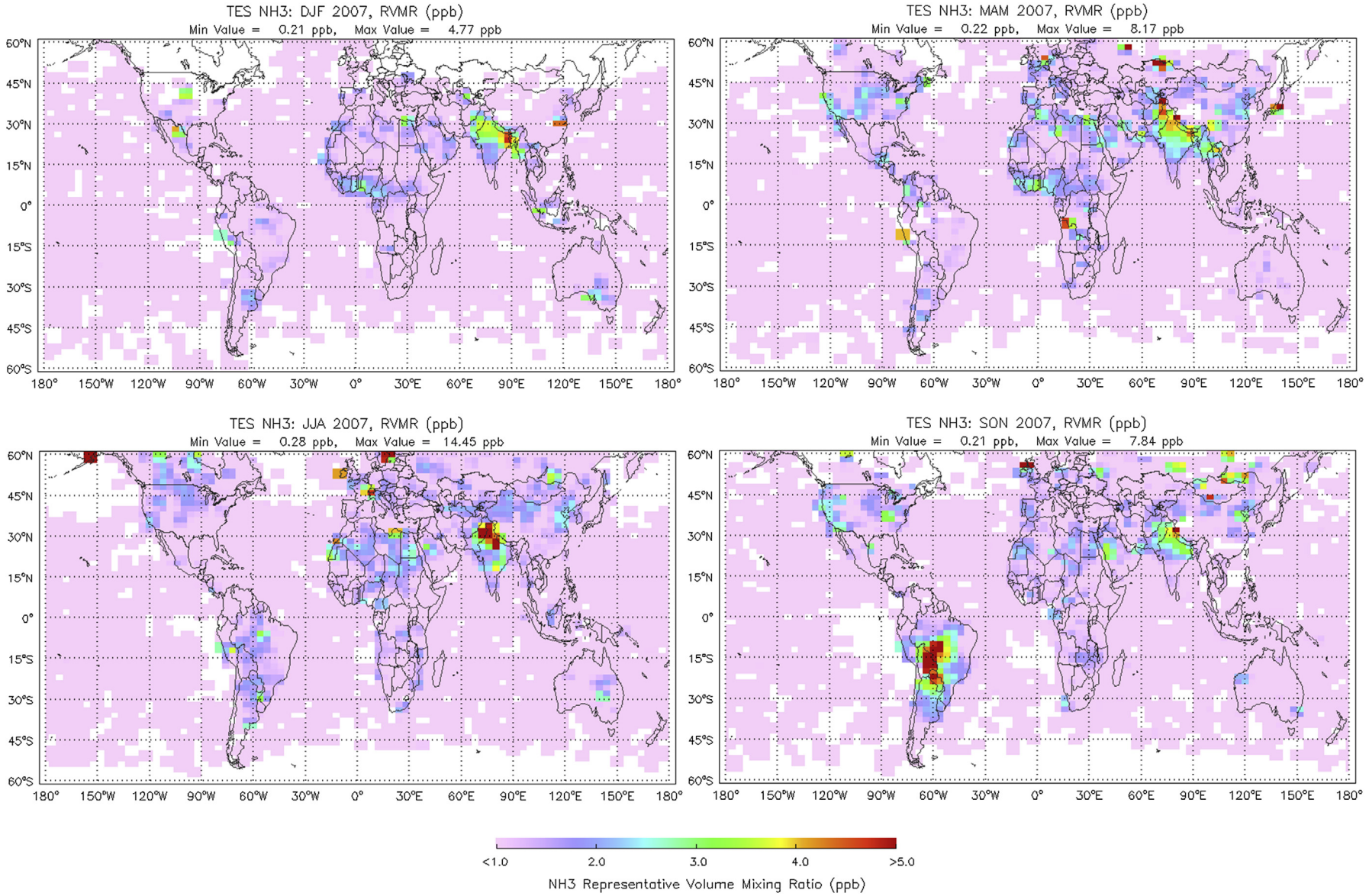

Fig. 4. Global averages of TES NH_3 RVMR for four seasons in 2007. Data are averaged over 2° latitude by 4° longitude bins inversely weighted by the error in RVMR and distance to the center of the bin boxes.

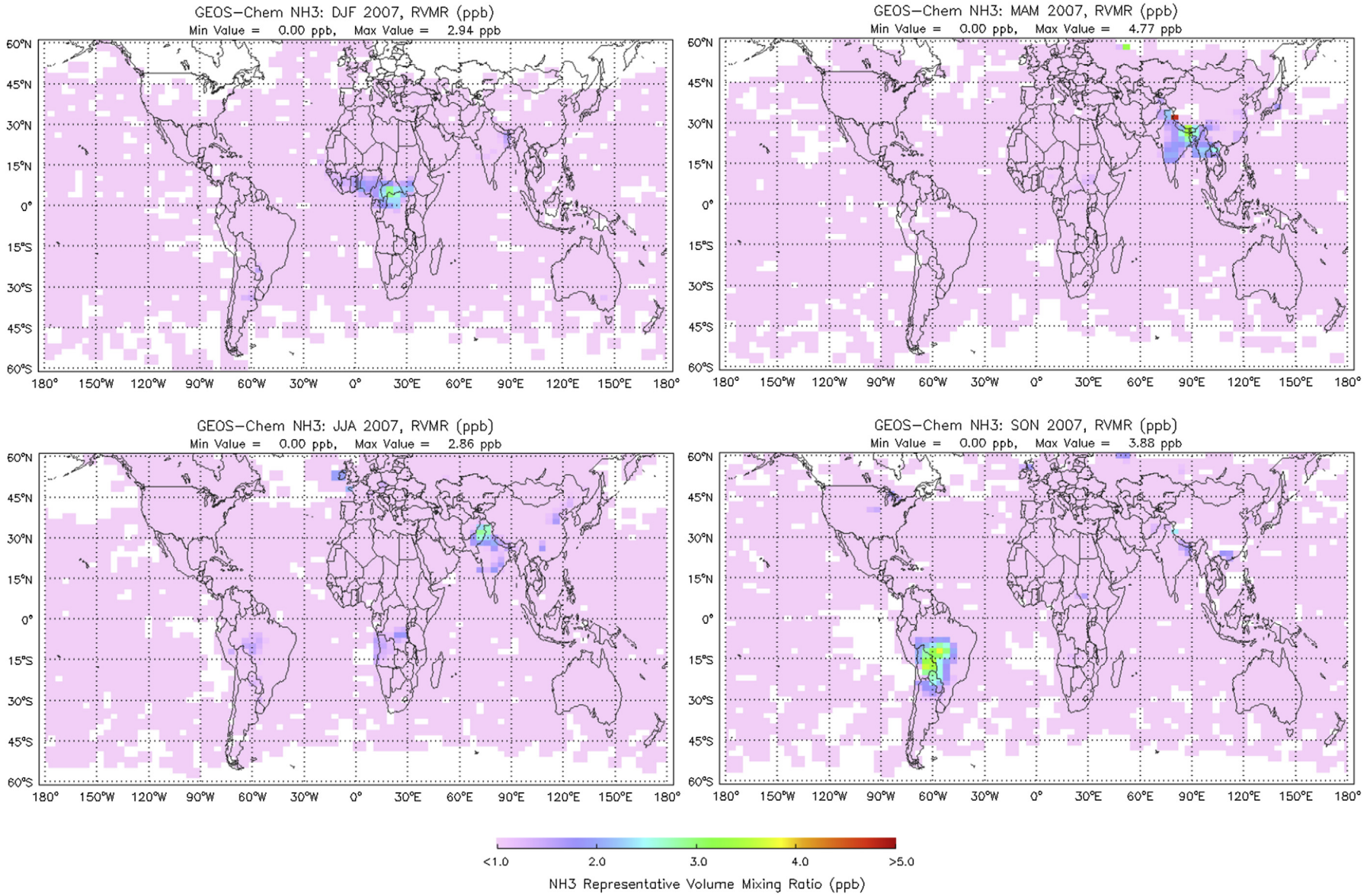

Fig. 5. Global averages of GEOS-Chem NH_3 RVMR for four seasons in 2007. Model data are sampled at TES observation locations and times; RVMR are calculated after TES observation operators are applied; Data are averaged over 2° latitude by 4° longitude bins.

3. Global distributions

Here we examine the global distributions of CO and NH_3 from TES and GEOS-Chem for 2007. All data discussed in the following sections are grouped into four seasons, Jan–Feb and Dec (DJF), Mar–May (MAM), June–Aug (JJA), and Sept–Nov (SON). The GEOS-Chem model data are sampled at TES observation locations and times.

3.1. TES/GEOS-Chem CO distributions

TES observed and GEOS-Chem modeled CO RVMR global distribution maps are shown in Figs. 2 and 3 for the four seasons of 2007. These maps are generated following the TES L3 algorithm (Luo, 2005). Although the GEOS-Chem CO simulation results are generally lower compared to TES CO observations in the northern hemisphere (−27 to −16 ppb +/−33 to 45 ppb in global mean differences), which is believed due to weak emission or vertical transport (Kopacz et al., 2010), the TES and GEOS-Chem seasonal variations and their CO enhancement regions agree well. In the northern hemisphere, emitted CO is accumulated in winter–spring due to its longer lifetime in those seasons, which is typically a few weeks, whereas in the summer the lifetime is just a few days. The noticeable features shown in both the TES and GEOS-Chem seasonal maps include enhanced CO due to biomass burning in the winter–spring of North-Central Africa (DJF) and South-Central Africa (JJA) respectively, and the spring in South America (SON). The high CO over South-East Asia in spring (MAM) is also due to fires. These fire events tend to occur every year with different relative numbers and strength as indicated by MODIS fire maps (Justice et al., 2002). The enhanced CO over large areas of China and India seen in both TES and GEOS-Chem maps, especially from winter to late spring (DJF and MAM), is due to the accumulation effect from industry, traffic, and agricultural activities in these two developing countries with large population densities (Kopacz et al., 2009; Zhang et al., 2009; van der Werf et al., 2010).

3.2. TES/GEOS-Chem NH_3 distributions

Global NH_3 RVMR data are derived from TES observations and GEOS-Chem simulations with the TES observation operator applied (Equation (3)). Figs. 4 and 5 show the maps of TES and GEOS-Chem NH_3 RVMR averaged for the four seasons of 2007. Observations and model global distributions present similarities and differences in the NH_3 concentrations. Overall, compared to TES RVMR values, the GEOS-Chem data are lower, which is consistent with previous global comparisons (e.g. Shephard et al., 2011). The global GEOS-Chem NH_3 RVMR is biased low compared to TES with seasonal mean differences of −0.92 to −0.8 ppb +/−1.24–1.58 ppb. TES data also show larger variability which might be due to the impact of retrieval errors (which can range from 10 to 40%) and/or the different spatial sampling of the highly variable NH_3 concentrations by TES (8.3 × 5.3 km) and GEOS-Chem (2° latitude × 2.5° longitude). Some outlier hot spots are believed due to local events at the times of the observations.

In general the seasonality and the enhanced NH_3 regions are seen in both TES and GEOS-Chem. Some of the most noticeable NH_3 enhancements occur in the biomass burning regions and seasons: South America in spring (SON), the winter–spring of North-Central Africa (DJF) and South-Central Africa (JJA), and the spring of South East-Asia (MAM). The other noticeable NH_3 enhancements are over Northern India and Northern-Central China. These high NH_3 values are seen year-round, especially in the TES observations. There are some differences in GEOS-Chem NH_3 compared to TES observations in northern high latitudes, e.g., Central Valley in California. These differences have been used to re-evaluate the NH_3 emission inputs in model simulations (Zhu et al., 2013).

4. NH_3:CO correlations

To investigate the NH_3:CO correlations in different source regimes, we examined seasonal NH_3 and CO distributions from TES observations and GEOS-Chem simulations described in Section 3 in regions where there are enhancements in either or both species. The model data used here are those sampled at TES observation locations and times. The selected areas include known biomass burning regions and high population density regions with enhanced CO or NH_3 sources dominated by human activities such as agriculture, industry, and traffic.

Fig. 6 shows the boundaries defined for six regions, NC and SC Africa, S America, Mid-US, SC Asia, and NC China. Among these regions, dry season biomass burnings are the dominant sources for elevated CO and NH_3 in NC and SC Africa, and S America regions. The mixture of agriculture, industrial, traffic activities and possible fire events in certain seasons are typically responsible for elevated CO and NH_3 in SC Asia, NC China and Mid-US regions.

In this section, we first analyze the GEOS-Chem model simulations of NH_3:CO for some of the above selected regions/seasons obtained by turning biomass burning on and off. The regional TES observations and GEOS-Chem simulations of NH_3–CO correlations are then examined and summarized in 4.2.

4.1. GEOS-Chem model simulations with and without biomass burning sources

The effects of biomass burning on the global distributions of NH_3 and CO are investigated by running the GEOS-Chem model with and without the biomass burning sources. TES observation geolocations and times are used to sample the model data. Fig. 7 contains the global results of the GEOS-Chem CO fields from the simulations for 2007 with and without biomass burning sources. The data were derived by taking the differences between the run with all pollution sources (control run) and the run with biomass burning sources turned off. Three biomass burning dominated season/regions (see Fig. 6) were selected based on the difference in the CO in Fig. 7: North-Central Africa (DJF), South-Central Africa (JJA), and South America (SON).

We use the model results to illustrate the expected NH_3:CO relationships in two categories of regions: biomass burning dominated and non-biomass burning. Fig. 8 shows NH_3:CO scatter plots from model simulations created from the difference between the control and the no biomass burning sources simulations at the TES sampling. These results show that under biomass burning conditions NH_3 and CO show strong positive correlations (0.65–0.8) and a NH_3:CO ratio (NH_3 enhancement ratio relative to CO) of 0.010–0.013.

In addition to regions with significant biomass burning contributions, it is also interesting to look at NH_3:CO correlations in regions with elevated emissions (i.e. industrial or agricultural emissions) and no significant biomass burning sources. One such non-biomass burning region is SC Asia; the NH_3:CO correlation plots using model results without biomass burning sources for this region for all 4 seasons are shown in Fig. 9. In these cases, the NH_3:CO RVMR ratios range from 0.02 to 0.08 and the correlations from 0.35 to 0.60, a distinctly different result from that of biomass burning cases shown in Fig. 8. These GEOS-Chem simulations with and without biomass burning show that the NH_3:CO ratios can be utilized as a metric to evaluate model performance against TES measurements, which is presented in the next section for 2007.

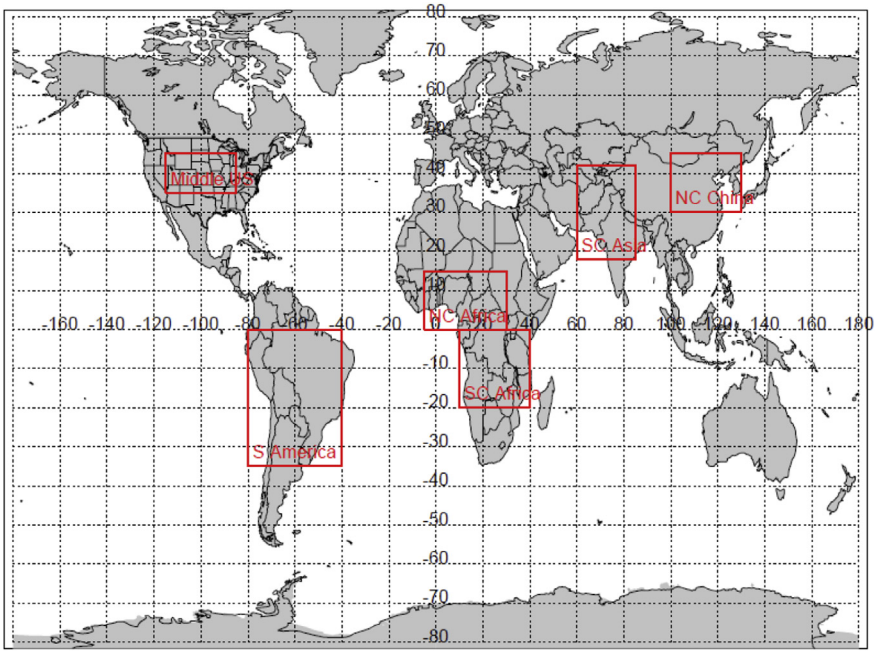

Fig. 6. Data from the six regions shown in the boxes are selected to examine the correlations between NH_3 and CO from TES and GEOS-Chem.

4.2. Correlations from TES and GEOS-Chem data by region

In this section the TES and GEOS-Chem NH_3:CO correlations are examined for the various regions and seasons. The NH_3:CO ratio is also referred to as the NH_3 enhancement ratio relative to CO derived over fires (e.g., Coheur et al., 2009; R'Honi et al., 2013). Fig. 10 shows NH_3:CO correlation plots for South America in MAM and SON of 2007. There are two distinct behaviors in the NH_3 and CO relationships. During the southern hemisphere summer–fall seasons (e.g., MAM), no obvious fire events occurred, as indicated by the low CO RVMR values. The low-moderate NH_3 RVMR values are most likely due to agriculture activities. During the southern hemisphere winter–spring seasons (e.g., SON), there were strong fire events. This biomass burning enhancements in CO and NH_3 emissions is demonstrated by their strong positive correlation shown in Fig. 10. The relationship exists in both TES and GEOS-Chem data. The correlations for the other two seasons (not shown) demonstrated a mixture of the two types of relationships.

Other regions with similar characteristics to South America are NC and SC Africa. Fig. 11 shows NH_3 vs CO in the winter and summer of 2007 for the NC Africa region. In winter months, the high CO and NH_3 are dominated by the biomass burning sources in the region. Thus, the two species demonstrate strong positive correlations. In the summer months when there is little expected biomass burning emissions, we see low CO values and low-moderate NH_3 values. Again, both TES and GEOS-Chem model data show similar relationships between CO and NH_3 in this region, indicating that the model provides a good representation of these species in this region for each season.

For the regions and seasons in which fire events are not the dominating sources of NH_3 and CO, industrial and agricultural activities are the main sources of CO and NH_3: for example SC Asia and NC China. Fig. 12 shows NH_3 versus CO for all four seasons of 2007 from the data in SC Asia. For most of the year CO and NH_3 are positively correlated with large values, indicating strong emission sources for both pollutants. In the summer months (JJA), the CO amount is relatively small compared to the other seasons due to the stronger sink for CO via reactions with enhanced OH. It is important to note that the lifetime for NH_3 is often on the order of hours, thus the year-round high abundances of NH_3 indicate strong emission fluxes within the region. These characteristics in NH_3:CO correlations that are distinguishable from the fire dominated regions, e.g., Figs. 10 and 11, are displayed in both TES and GEOS-Chem model data.

The NH_3:CO ratios and their correlation coefficients for all six regions outlined in Fig. 6 and four seasons are summarized in Table 1. Two categories are listed: (i) "biomass burning" (BB) and (ii) "anthropogenic source dominated high NH_3" (High NH_3) cases. Both TES observations and GEOS-Chem model results are provided. No data are presented for regions/seasons for which the two species are not enhanced and not obviously correlated, e.g., MAM of S America in Fig. 10 and JJA of N Africa in Fig. 11. As previously demonstrated (Figs. 10 and 11), the strongest positive correlations between NH_3 and CO typically occur in fire regions and seasons, for example South America in the austral late winter and spring, and NC and SC Africa in their dry seasons. In other regions, NH_3 and CO are much more weakly correlated due to their different emission sources and lifetimes. In Table 1, we highlighted (red) those cases with reasonably high correlations for the two categories. In general, although GEOS-Chem under-estimated both NH_3 and CO globally compared to TES observations as discussed in sections 3.1 and 3.2, the correlations from the model agree reasonably well with those from TES.

The ratios of NH_3:CO (the slopes of the NH_3 vs CO regression lines for the given locations shown in Figs. 10–12) listed in Table 1 are used to calculate the averaged values for the two categories, the "biomass burning" (BB) and "anthropogenic source dominated high NH_3" (high NH_3) cases. For the "biomass burning" cases, average NH_3:CO values are 0.015 ± 0.001 from TES and 0.013 ± 0.001 from GEOS-Chem, which is consistent with the GEOS-Chem simulated biomass burning signal shown in Fig. 8. This average TES NH_3:CO ratio from the biomass burning cases lies within the range of NH_3:CO values from different biomass burning types recently reported by Akagi et al. (2011) of 0.014 (tropical forest), 0.008 (Savanna), 0.026 (Crop Residue), 0.011 (Pasture Maintenance), 0.021 (Boreal Forest), 0.009 (Temperate Forest), 0.020 (Extra

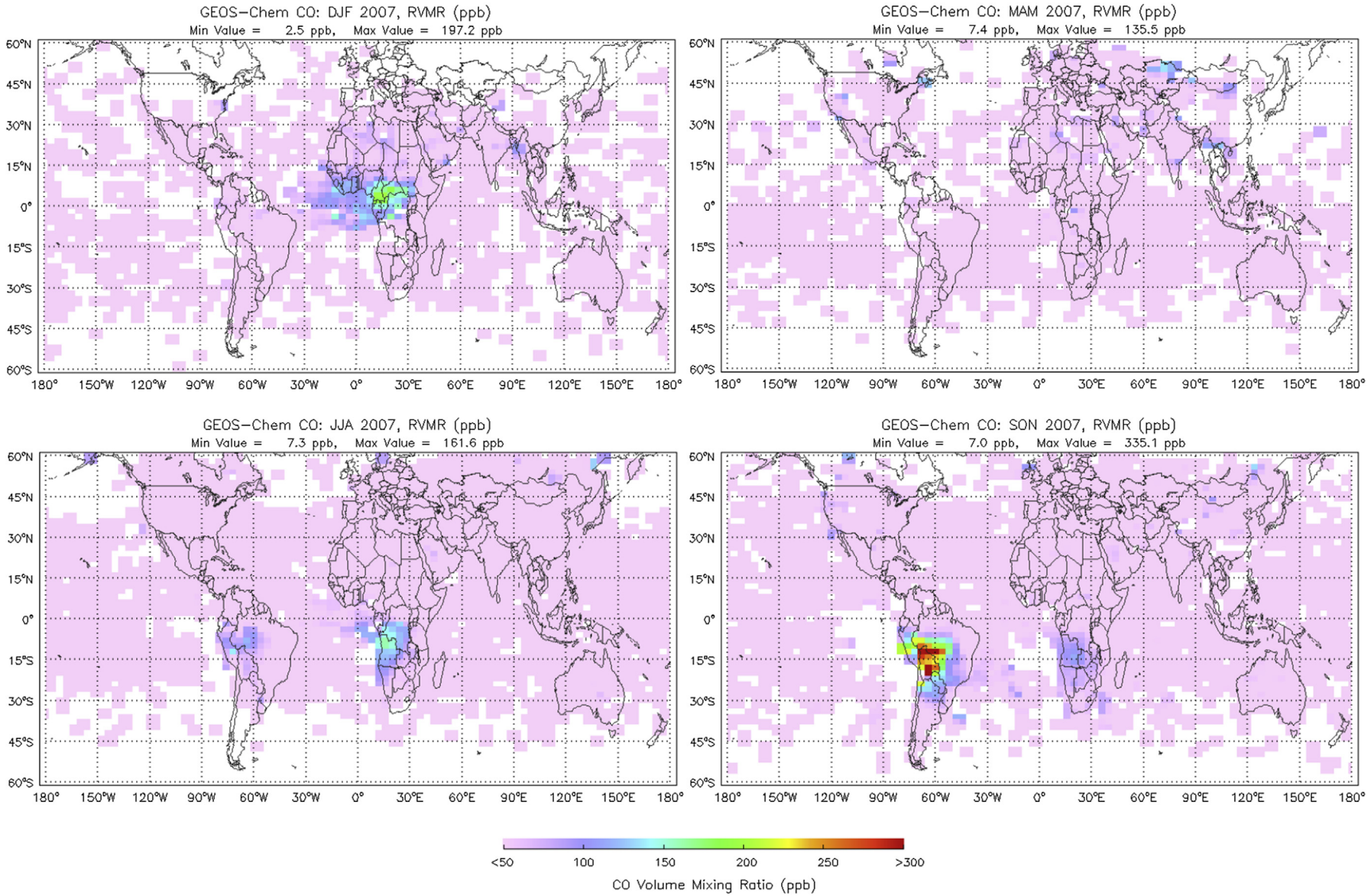

Fig. 7. Similar to Fig. 3, but showing the differences in GEOS-Chem CO simulations between the control simulation (including all sources, Fig. 3) and a simulation without biomass burning sources for four seasons in 2007.

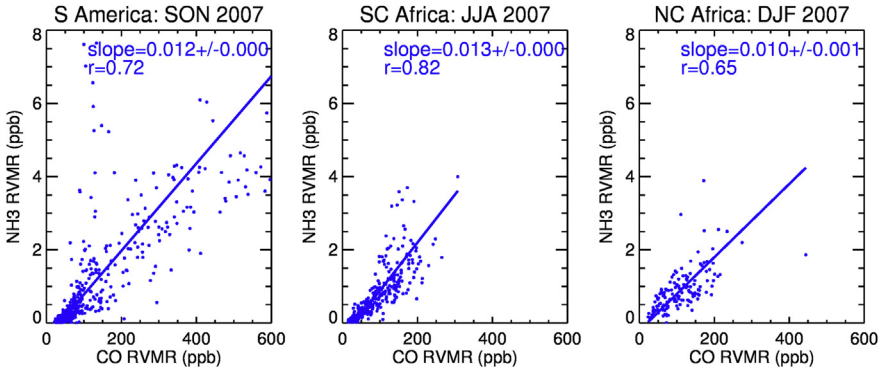

Fig. 8. GEOS-Chem model fire-only simulations of NH_3 RVMR vs CO RVMR for the three regions shown in Fig. 6 dominated by biomass burning. The model results used to derive RVMR are the differences between two model runs: the control (with all sources) and the 'no biomass burning source' simulations. Model points are those sampled at TES observation locations and times.

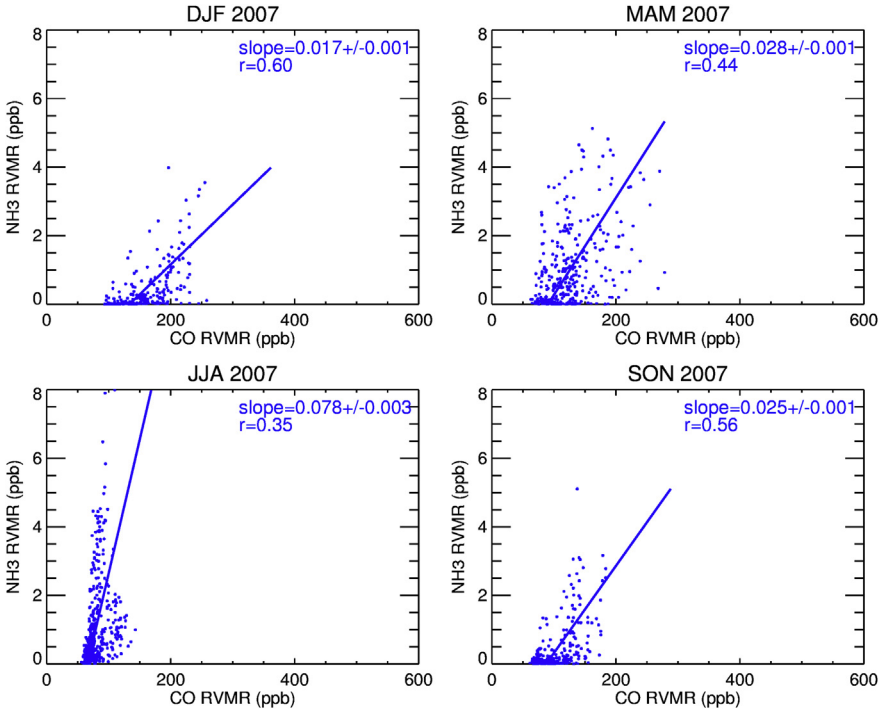

Fig. 9. GEOS-Chem model simulations of NH_3 RVMR vs CO RVMR for SC Asia region shown in Fig. 6. The model results used to derive RVMRs are the VMR profiles simulated without biomass burning source.

tropical Forest), and also values reported by Paton-Walsh et al. (2014) of 0.013 for temperate forest, and Smith et al. (2014) of 0.008 for tropical savanna fires. For anthropogenic source dominated "high NH_3" cases, the ratios of the two species are 0.051 ± 0.003 from TES and 0.036 ± 0.002 from GEOS-Chem, which is consistent with the expected larger ratio values from the GEOS-Chem simulations shown in Fig. 9 for conditions without significant biomass burning emission contributions. The slightly lower values of NH_3:CO ratio in GEOS-Chem model compared to TES observations indicate a possible low emission inventories in NH_3 used in model simulations (Zhu et al., 2013).

Extending this analysis to finer scales and to a more quantitative result is more challenging due to the sparseness of TES data. The sources of the TES observations in each region shown in Fig. 6 can be a mixture of urban and rural areas or cities and farms. For example, in the mid-US region, cities and livestock facilities are sparsely distributed within large agricultural areas; in the NC plain of China, there are populated cities and industrial factories embedded in agricultural areas. Even within some of the larger regions, the TES observations presented here are under or non-uniformly sampled. The regional/seasonal distributions could therefore be biased by events, e.g., a short term fire in a mixed source region. In many cases, the retrieval error, especially for NH_3, can be large compared with its variability in the region for a season. Some of these challenges should be overcome by more frequent and densely covered measurements in the future satellite observations.

5. Conclusions

TES global satellite observations of NH_3 and CO in 2007 are analyzed together with GEOS-Chem model simulations. The derived Representative Volume Mixing Ratios (RVMRs) for the two

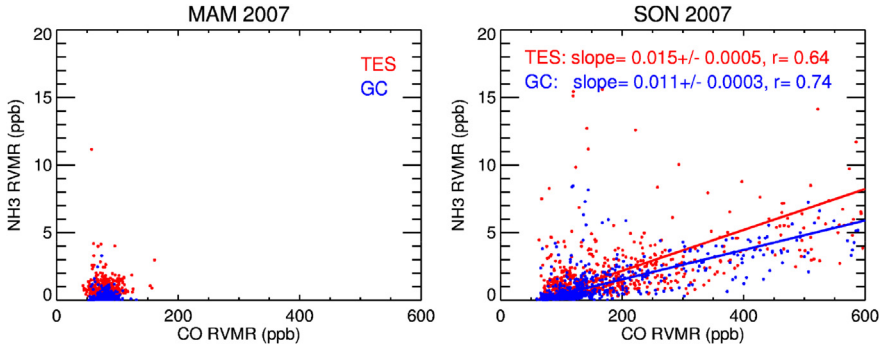

Fig. 10. Scatter plots of TES (red) and GEOS-Chem (blue) NH_3 RVMR vs CO RVMR for data in S America region (Fig. 6): (left panel) MAM 2007 and (right panel) the biomass burning season of SON 2007. (For interpretation of the references to color in this figure legend, the reader is referred to the web version of this article.)

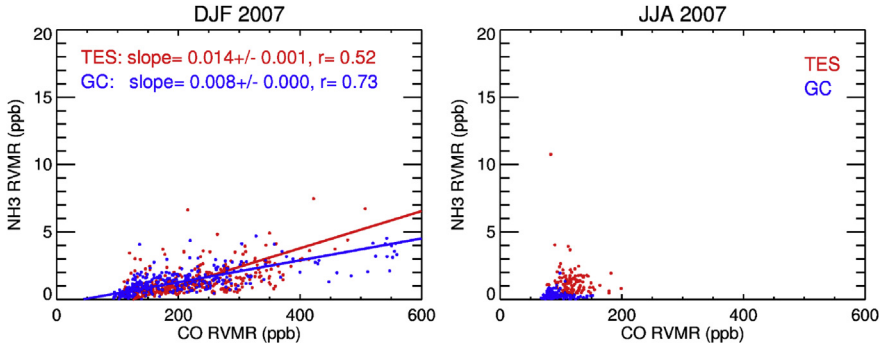

Fig. 11. Scatter plots of TES (red) and GEOS-Chem (blue) NH_3 RVMR vs CO RVMR for data in NC Africa region (Fig. 6): (left panel) Biomass burning season of DJF 2007 and (right panel) the non-biomass burning season of JJA 2007. (For interpretation of the references to color in this figure legend, the reader is referred to the web version of this article.)

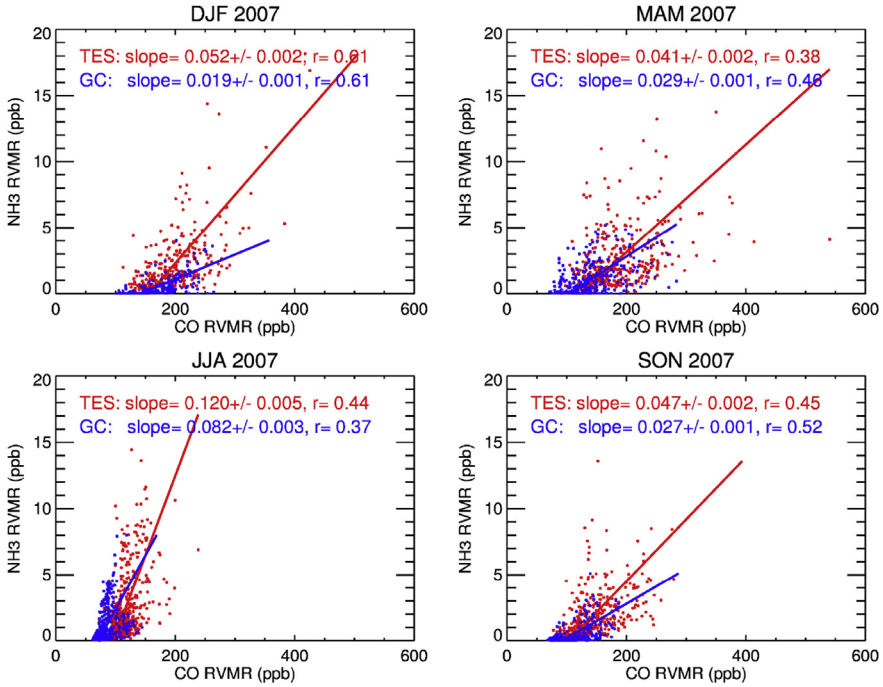

Fig. 12. Scatter plots of TES (red) and GEOS-Chem (blue) NH_3 RVMR vs CO RVMR from data in SC Asia region (Fig. 6) for four seasons. (For interpretation of the references to color in this figure legend, the reader is referred to the web version of this article.)

Table 1
Correlation coefficients of NH_3:CO RVMR and the slopes of reduced-major-axis regression lines for six regions and four seasons from TES observations and GEOS-Chem simulations from 2007; data in red have stronger correlations and noticeable enhancement in one or both species; unfilled cells indicate no enhancements in observed NH_3 and CO or weak/non-exist in their correlations).

Region	Season	TES		GC		Class
		Slope	Corr Coef	Slope	Corr Coef	
SC Asia	DJF	0.052±0.002	0.61	0.019±0.001	0.61	High NH_3
	MAM	0.041 ±0.002	0.38	0.029±0.001	0.46	High NH_3
	JJA	0.120 ±0.005	0.44	0.082 ±0.003	0.37	High NH_3
	SON	0.047±0.002	0.45	0.027±0.001	0.52	High NH_3
NC China	DJF					
	MAM	0.015±0.001	0.24	0.017±0.002	0.14	High NH_3
	JJA	0.018±0.001	0.09	0.032 ±0.001	0.45	High NH_3
	SON	0.038±0.001	0.12	0.026±0.002	0.44	High NH_3
Mid US	DJF					
	MAM					
	JJA	0.049±0.002	0.28	0.041 ±0.002	0.34	High NH_3
	SON	0.082±0.009	0.12	0.048±0.004	0.55	High NH_3
Average		**0.051±0.003**		**0.036±0.002**		**High NH_3**
S America	DJF					
	MAM					
	JJA					
	SON	0.015±0.000	0.64	0.011±0.000	0.74	BB
SC Africa	DJF					
	MAM					
	JJA	0.013±0.001	0.11	0.014±0.001	0.62	BB
	SON	0.011±0.001	0.19	0.016±0.001	0.70	BB
NC Africa	DJF	0.014±0.001	0.52	0.008±0.000	0.73	BB
	MAM	0.023±0.001	0.38	0.017±0.001	0.37	BB
	JJA					
	SON					
Average		**0.015±0.001**		**0.013±0.001**		**BB**

species are used in this study. Data from 2007 were selected as it was a year with strong biomass burning events in the tropics. The global/seasonal distributions of the two species are characterized by correlated enhancements in regions where they have common biomass burning or other incomplete combustion sources, and weak or non-existent correlated enhancements where the sources are distinct. In biomass burning regions, the two species show strong positive correlations, with NH_3:CO ratios of 0.015 (TES) and 0.013 (GEOS-Chem). We gained further insight on the relationship between NH_3 and CO by running the GEOS-Chem model with and without biomass burning sources. In other regions or seasons, the two species show much weaker correlations. In regions of high population density, known heavy traffic, dense livestock or intense agricultural activities (e.g. SC Asia and NC China) the two species show positive correlations with higher NH_3:CO ratios: 0.051 (TES) and 0.036 (GEOS-Chem). Although GEOS-Chem simulations of NH_3 and CO RVMRs are lower than the TES retrieved values, the global distribution patterns agree with TES, indicating good understanding of the source regions and seasonal enhancements of the two species globally over these large regions. The determination of the NH_3:CO ratios are useful in more accurately determining the emission inventories of NH_3 globally, especially as the CO emission inventories are better known. While further constraints on ecosystem and process specific emissions would indeed be of value, given the large uncertainties that presently persist for NH_3 emissions across all sources, the constraints from NH_3:CO ratios on biomass burning sources alone can provide useful information, even in situations where global measurements of NH_3 are available from instruments such as TES (Shephard et al., 2011), Infrared Atmospheric Sounding Interferometer (IASI) (Van Damme et al., 2014), and Cross-track Infrared Sounder (CrIS) (Shephard and Cady-Pereira, 2014). For example, the NH_3:CO ratios offer additional insight on "hot-spots" in global NH_3 concentrations often seen at high-latitudes (e.g. Russia and Canada), that are often, but not always, from biomass burning events.

In regions with a complex variety of potential sources of NH_3 and CO emissions it is challenging to analyze their relative abundances given the TES sampling frequency and retrieval precision. High spatial-temporal resolution observations of NH_3, CO and other species with high precision are recommended for future air quality satellite instrument definitions.

Acknowledgments

Research was partially supported by the Jet Propulsion Laboratory, California Institute of Technology under contract to the

National Aeronautics and Space Administration (NASA). We also recognize support from NASA ACMAP NNX10AG63G and EPA-STAR RD83455901. SC was supported by an appointment to the Research Participation Program at the U.S. EPA, administered by the Oak Ridge Institute for Science and Education. Although this paper has been reviewed by EPA and approved for publication, it does not necessarily reflect official EPA agency views or policies.

References

Akagi, S.K., Yokelson, R.J., Wiedinmyer, C., Alvarado, M.J., Reid, J.S., Karl, T., Crounse, J.D., Wennberg, P.O., 2011. Emission factors for open and domestic biomass burning for use in atmospheric models. Atmos. Chem. Phys. 11, 4039–4072. http://dx.doi.org/10.5194/acp-11-4039-2011.

Alvarado, M.J., Payne, V.H., Mlawer, E.J., Uymin, G., Shephard, M.W., Cady-Pereira, K.E., Delamere, J.S., Moncet, J.L., 2013. Performance of the Line-By-Line Radiative Transfer Model (LBLRTM) for temperature, water vapor, and trace gas retrievals: recent updates evaluated with IASI case studies. Atmos. Chem. Phys. 13, 6687–6711. http://dx.doi.org/10.5194/acp-13-6687-2013.

Beer, R., 2006. TES on the aura mission: scientific objectives, measurements, and analysis overview. IEEE Trans. Geosci. Remote Sens. 44 (5), 1102–1105. http://dx.doi.org/10.1109/TGRS.2005.863716.

Beusen, A.H.W., Bouwman, A.F., Heuberger, P.S.C., Van Drecht, G., Van Der Hoek, K.W., 2008. Bottom-up uncertainty estimates of global ammonia emissions from global agricultural production systems. Atmos. Environ. 42 (24), 6067–6077. http://dx.doi.org/10.1016/j.atmosenv.2008.03.044.

Binkowski, F., Roselle, S., 2003. Models-3 Community Multiscale Air Quality (CMAQ) model aerosol component – 1. Model description. J. Geophys. Res. 108 (D6), 4183–4201. http://dx.doi.org/10.1029/2001JD001409.

Bouwman, A.F., Lee, D.S., Asman, W.A.H., Dentener, F.J., Van Der Hoek, K.W., Olivier, J.G.J., 1997. A global high-resolution emission inventory for ammonia. Glob. Biogeochem. Cycles 11 (4), 561. http://dx.doi.org/10.1029/97GB02266.

Bowman, K.W., Rodgers, C.D., Kulawik, S.S., Worden, J., Sarkissian, E., Osterman, G., Steck, T., Lou, M., Eldering, A., Shephard, M., Worden, H., Lampel, M., Clough, S., Brown, P., Rinsland, C., Gunson, M., Beer, R., 2006. Tropospheric emission spectrometer: retrieval method and error analysis. IEEE Trans. Geosci. Remote Sens. 44 (5), 1297–1307. http://dx.doi.org/10.1109/TGRS.2006.871234.

Boynard, A., Clerbaux, C., Clarisse, L., Safieddine, S., Pommier, M., Van Damme, M., Bauduin, S., Oudot, C., Hadji-Lazaro, J., Hurtmans, D., Coheur, P.-F., 2014. First simultaneous space measurements of atmospheric pollutants in the boundary layer from IASI: a case study in the North China Plain. Geophys. Res. Lett. 41 (2), 645–651. http://dx.doi.org/10.1002/2013GL058333.

Cady-Pereira, K.E., Shephard, M.W., Henze, D.K., Zhu, L., Wrotny, J., Nowak, J., Wisthaler, A., Sun, K., Scarino, A.J., Pinder, R.W., Luo, M., 2013. Ammonia Measurements by the NASA Tropospheric Emission Spectrometer (TES) and the NPP Suomi Cross-track Infrared Sounder (CrIS). Presentation at the AGU 2013 Fall Meeting, San Francisco, California.

Clarisse, L., Clerbaux, C., Dentener, F., Hurtmans, D., Coheur, P.-F., 2009. Global ammonia distribution derived from infrared satellite observations. Nat. Geosci. 2 (7), 479–483. http://dx.doi.org/10.1038/ngeo551.

Clarisse, L., Shephard, M.W., Dentener, F., Hurtmans, D., Cady-Pereira, K., Karagulian, F., Damme, M.V., Clerbaux, C., Coheur, P.-F., 2010. Satellite monitoring of ammonia: a case study of the San Joaquin Valley. J. Geophys. Res. 115 (13).

Clough, S.A., Shephard, M.W., Worden, J., Brown, P.D., Worden, H.M., Luo, M., Rodgers, C.D., Rinsland, C.P., Goldman, A., Brown, L., Kulawik, S.S., Eldering, A., Lampel, M., Osterman, G., Beer, R., Bowman, K., Cady-Pereira, K.E., Mlawer, E.J., 2006. Forward model and Jacobians for tropospheric emission spectrometer retrievals. IEEE Trans. Geosci. Remote Sens. 44 (5), 1308–1323. http://dx.doi.org/10.1109/TGRS.2005.860986.

Coheur, P.-F., Clarisse, L., Turquety, S., Hurtmans, D., Clerbaux, C., 2009. IASI measurements of reactive trace species in biomass burning plumes. Atmos. Chem. Phys. 9, 5655–5667. http://dx.doi.org/10.5194/acp-9-5655-2009.

Connor, T.C., Shephard, M.W., Payne, V.H., Cady-Pereira, K.E., Kulawik, S.S., Luo, M., Osterman, G., Lampel, M., 2011. Long-term stability of TES satellite radiance measurements. Atmos. Meas. Tech. 4 (7), 1481–1490. http://dx.doi.org/10.5194/amt-4-1481-2011.

Crouse, D.L., Peters, P.A., van Donkelaar, A., Goldberg, M.S., Villeneuve, P.J., Brion, O., Khan, S., Atari, D.O., Jerrett, M., Pope, C.A., Brauer, M., Brook, J.R., Martin, R.V., Stieb, D., Burnett, R.T., 2012. Risk of nonaccidental and cardiovascular mortality in relation to long-term exposure to low concentrations of fine particulate matter: a Canadian national-level cohort study. Environ. Health Perspect. 120 (5), 708–714. http://dx.doi.org/10.1289/ehp.1104049.

Edwards, D.P., Emmons, L.K., Hauglustaine, D.A., Chu, D.A., Gille, J.C., Kaufman, Y.J., Pétron, G., Yurganov, L.N., Giglio, L., Deeter, M.N., Yudin, V., Ziskin, D.C., Warner, J., Lamarque, J.-F., Francis, G.L., Ho, S.P., Mao, D., Chen, J., Grechko, E.I., Drummond, J.R., 2004. Observations of carbon monoxide and aerosols from the Terra satellite: northern Hemisphere variability. J. Geophys. Res. 109 (D24), D24202. http://dx.doi.org/10.1029/2004JD004727.

Edwards, D.P., Petron, G., Novelli, P.C., Emmons, L.K., Gille, J.C., Drummond, J.R., 2006. Southern Hemisphere carbon monoxide interannual variability observed by Terra/Measurement of Pollution in the Troposphere (MOPITT). J. Geophys. Res. 111 (D16), D16303. http://dx.doi.org/10.1029/2006JD007079.

Forster, P., Ramaswamy, V., Artaxo, P., Berntsen, T., Betts, R., Fahey, D., Haywood, J., Lean, J., Lowe, D., Myhre, G., 2007. Climate Change 2007: the Physical Science Basis. Contribution of Working Group I. In: Fourth Assessment Report of the Intergovernmental Panel on Climate Change. Cambridge University Press.

George, M., Clerbaux, C., Hurtmans, D., Turquety, S., Coheur, P.-F., Pommier, M., Hadji-Lazaro, J., Edwards, D.P., Worden, H., Luo, M., Rinsland, C., McMillan, W., 2009. Carbon monoxide distributions from the IASI/METOP mission: evaluation with other space-borne remote sensors. Atmos. Chem. Phys. 9, 8317–8330. http://dx.doi.org/10.5194/acp-9-8317-2009.

Hegg, D.A., Radke, L.F., Hobbs, P.V., Riggan, P.J., 1988. Ammonia emissions from biomass burning. Geophys. Res. Lett. 15 (4), 335–337. http://dx.doi.org/10.1029/GL015i004p00335.

Herman, R.L., Kulawik, S.S. (Eds.), 2013. Tropospheric Emission Spectrometer TES Level 2 (L2) Data User's Guide, D-38042, Version 6.0. Jet Propulsion Laboratory, California Institute of Technology, Pasadena, CA. Available at: http://tes.jpl.nasa.gov/documents.

Ho, S.-P., Edwards, D.P., Gille, J.C., Luo, M., Osterman, G.B., Kulawik, S.S., Worden, H., 2009. A global comparison of carbon monoxide profiles and column amounts from Tropospheric Emission Spectrometer (TES) and Measurements of Pollution in the Troposphere (MOPITT). J. Geophys. Res. 114 (D21), D21307. http://dx.doi.org/10.1029/2009JD012242.

Justice, C.O., Giglio, L., Korontzi, S., Owens, J., Morisette, J.T., Roy, D., Descloitres, J., Alleaume, S., Petitcolin, F., Kaufman, Y., 2002. The MODIS Fire Products, the Moderate Resolution Imaging Spectroradiometer (MODIS): a New Generation of Land Surface Monitoring, vol. 83(1–2), pp. 244–262.

Kopacz, M., Jacob, D.J., Henze, D.K., Heald, C.L., Streets, D.G., Zhang, Q., 2009. Comparison of adjoint and analytical Bayesian inversion methods for constraining Asian sources of carbon monoxide using satellite (MOPITT) measurements of CO columns. J. Geophys. Res. 114, D04305. http://dx.doi.org/10.1029/2007JD009264.

Kopacz, M., Jacob, D.J., Fisher, J.A., Logan, J.A., Zhang, L., Megretskaia, I.A., Yantosca, R.M., Singh, K., Henze, D.K., Burrows, J.P., Buchwitz, M., Khlystova, I., McMillan, W.W., Gille, J.C., Edwards, D.P., Eldering, A., Thouret, V., Nedelec, P., 2010. Global estimates of CO sources with high resolution by adjoint inversion of multiple satellite datasets (MOPITT, AIRS, SCIAMACHY, TES). Atmos. Chem. Phys. 10 (3), 855–876. http://dx.doi.org/10.5194/acp-10-855-2010.

Kuhns, H., Knipping, E.M., Vukovich, J.M., 2005. Development of a United States-Mexico emissions inventory for the Big Bend Regional Aerosol and Visibility Observational (BRAVO) study. J. Air Waste Manage. Assoc. 55 (5), 677–692.

Langridge, J.M., Lack, D., Brock, C.A., Bahreini, R., Middlebrook, A.M., Neuman, J.A., Nowak, J.B., Perring, A.E., Schwarz, J.P., Spackman, J.R., Holloway, J.S., Pollack, I.B., Ryerson, T.B., Roberts, J.M., Warneke, C., de Gouw, J.A., Trainer, M.K., Murphy, D.M., 2012. Evolution of aerosol properties impacting visibility and direct climate forcing in an ammonia-rich urban environment. J. Geophys. Res. 117 (D21) http://dx.doi.org/10.1029/2011JD017116. D00V11–n–a.

Liang, Q., Jaeglé, L., Jaffe, D.A., Weiss Penzias, P., Heckman, A., Snow, J.A., 2004. Long-range transport of Asian pollution to the northeast Pacific: seasonal variations and transport pathways of carbon monoxide. J. Geophys. Res. 109 (D23), D23S07. http://dx.doi.org/10.1029/2003JD004402.

Liu, H., Jacob, D.J., Bey, I., Yantosca, R.M., 2001. Constraints from 210Pb and 7Be on wet deposition and transport in a global three-dimensional chemical tracer model driven by assimilated meteorological fields. J. Geophys. Res. 106 (D11), 12109–12128. http://dx.doi.org/10.1029/2000JD900839.

Lopez, J.P., Luo, M., Christensen, L.E., Loewenstein, M., Jost, H., Webster, C.R., Osterman, G., 2008. TES carbon monoxide validation during two AVE campaigns using the Argus and ALIAS instruments on NASA's WB-57F. J. Geophys. Res. 113 (D16), D16S47. http://dx.doi.org/10.1029/2007JD008811.

Luo, M., 2005. Tropospheric Emission Spectrometer (TES) Level 3 (L3) Algorithm, Requirements and Products, JPL D-26534. Jet Propulsion Laboratory, California Institute of Technology, Pasadena, CA. Available at: http://tes.jpl.nasa.gov/documents.

Luo, M., Rinsland, C.P., Rodgers, C.D., Logan, J.A., Worden, H., Kulawik, S., Eldering, A., Goldman, A., Shephard, M.W., Gunson, M., Lampel, M., 2007a. Comparison of carbon monoxide measurements by TES and MOPITT: influence of a priori data and instrument characteristics on nadir atmospheric species retrievals. J. Geophys. Res. 112 (D9), D09303. http://dx.doi.org/10.1029/2006JD007663.

Luo, M., Rinsland, C., Fisher, B., Sachse, G., Diskin, G., Logan, J., Worden, H., Kulawik, S., Osterman, G., Eldering, A., Herman, R., Shephard, M., 2007b. TES carbon monoxide validation with DACOM aircraft measurements during INTEX-B 2006. J. Geophys. Res. 112 (D24), D24S48. http://dx.doi.org/10.1029/2007JD008803.

Olivier, J.G.J., Berdowski, J.J.M., 2001. Global emissions sources and sinks. In: Berdowski, J., Guicherit, R., Heij, B.J. (Eds.), The Climate System. A.A. Balkema Publishers/Swets & Zeitlinger Publishers, Lisse, The Netherlands, ISBN 90 5809 255 0, pp. 33–78.

Park, R.J., Jacob, D., Field, B., Yantosca, R., Chin, M., 2004. Natural and transboundary pollution influences on sulfate-nitrate-ammonium aerosols in the United States: implications for policy. J. Geophys. Res. 109, D15204. http://dx.doi.org/10.1029/2003JD004473.

Paton-Walsh, C., Smith, T.E.L., Young, E.L., Griffith, D.W.T., Guérette, É.-A., 2014. New emission factors for Australian vegetation fires measured using open-path Fourier transform infrared spectroscopy – part 1: methods and Australian temperate forest fires. Atmos. Chem. Phys. 14, 11313–11333. http://dx.doi.org/10.5194/acp-14-11313-2014.

Pinder, R.W., Adams, P.J., Pandis, S.N., Gilliland, A.B., 2006. Temporally resolved ammonia emission inventories: current estimates, evaluation tools, and measurement needs. J. Geophys. Res. 111, D16310. http://dx.doi.org/10.1029/2005JD006603.

Pinder, R.W., Walker, J.T., Bash, J.O., Cady-Pereira, K.E., Henze, D.K., Luo, M., Osterman, G.B., Shephard, M.W., 2011. Quantifying spatial and seasonal variability in atmospheric ammonia with in situ and space-based observations. Geophys. Res. Lett. 38 (4) http://dx.doi.org/10.1029/2010GL046146.

Raub, J.A., Mathieu-Nolf, M., Hampson, N.B., Thom, S.R., 2000. Carbon monoxide poisoning — a public health perspective. Toxicology 145 (1), 1–14. http://dx.doi.org/10.1016/S0300-483X(99)00217-6.

Rinsland, C.P., Luo, M., Logan, J.A., Beer, R., Worden, H.M., Worden, J.R., Bowman, K., Kulawik, S.S., Rider, D., Osterman, G., Gunson, M., Goldman, A., Shephard, M., Clough, S.A., Rodgers, C., Lampel, M., Chiou, L., 2006. Nadir measurements of carbon monoxide distributions by the Tropospheric Emission Spectrometer instrument onboard the Aura Spacecraft: overview of analysis approach and examples of initial results. Geophys. Res. Lett. 33 (22), L22806. http://dx.doi.org/10.1029/2006GL027000.

R'Honi, Y., Clarisse, L., Clerbaux, C., Hurtmans, D., Duflot, V., Turquety, S., Ngadi, Y., Coheur, P.-F., 2013. Exceptional emissions of NH_3 and HCOOH in the 2010 Russian wildfires. Atmos. Chem. Phys. 13 (8), 4171–4181. http://dx.doi.org/10.5194/acp-13-4171-2013.

Rodgers, C.D., 2000. Inverse Methods for Atmospheric Sounding. World Scientific, Hackensack, NJ.

Shephard, M.W., Worden, H.M., Cady-Pereira, K.E., Lampel, M., Luo, M., Bowman, K.W., Sarkissian, E., Beer, R., Rider, D.M., Tobin, D.C., Revercomb, H.E., Fisher, B.M., Tremblay, D., Clough, S.A., Osterman, G.B., Gunson, M., 2008. Tropospheric emission spectrometer nadir spectral radiance comparisons. J. Geophys. Res. 113 (D15), D15S05. http://dx.doi.org/10.1029/2007JD008856.

Shephard, M.W., Cady-Pereira, K.E., Luo, M., Henze, D.K., Pinder, R.W., Walker, J.T., Rinsland, C.P., Bash, J.O., Zhu, L., Payne, V.H., Clarisse, L., 2011. TES ammonia retrieval strategy and global observations of the spatial and seasonal variability of ammonia. Atmos. Chem. Phys. 11 (20), 10743–10763. http://dx.doi.org/10.5194/acp-11-10743-2011.

Shephard, M.W., Cady-Pereira, K.E., 2014. Cross-track Infrared Sounder (CrIS) satellite observations of tropospheric ammonia. Atmos. Meas. Tech. Discuss. 7, 11379–11413. http://dx.doi.org/10.5194/amtd-7-11379-2014.

Smith, T.E.L., Paton-Walsh, C., Meyer, C.P., Cook, G.D., Maier, S.W., Russell-Smith, J., Wooster, M.J., Yates, C.P., 2014. New emission factors for Australian vegetation fires measured using open-path Fourier transform infrared spectroscopy – part 2: Australian tropical savanna fires. Atmos. Chem. Phys. Discuss. 14 (5), 6311–6360. http://dx.doi.org/10.5194/acpd-14-6311-2014.

Streets, D., Zhang, Q., Wang, L., He, K., Hao, J., Wu, Y., Tang, Y., Carmichael, G., 2006. Revisiting China's CO emissions after the Transport and Chemical Evolution over the Pacific (TRACE-P) mission: synthesis of inventories, atmospheric modeling, and observations. J. Geophys. Res. 111, D14306. http://dx.doi.org/10.1029/2006JD007118.

Van Damme, M., Clarisse, L., Heald, C.L., Hurtmans, D., Ngadi, Y., Clerbaux, C., Dolman, A.J., Erisman, J.W., Coheur, P.F., 2014. Global distributions, time series and error characterization of atmospheric ammonia (NH_3) from IASI satellite observations. Atmos. Chem. Phys. 14 (6), 2905–2922. http://dx.doi.org/10.5194/acp-14-2905-2014.

van der Werf, G.R., Randerson, J.T., Giglio, L., Collatz, G.J., Kasibhatla, P.S., Arellano Jr., A.F., 2006. Interannual variability in global biomass burning emissions from 1997 to 2004. Atmos. Chem. Phys. 6 (11), 3423–3441. http://dx.doi.org/10.5194/acp-6-3423-2006.

van der Werf, G.R., Randerson, J.T., Giglio, L., Collatz, G.J., Mu, M., Kasibhatla, P.S., Morton, D.C., DeFries, R.S., Jin, Y., van Leeuwen, T.T., 2010. Global fire emissions and the contribution of deforestation, savanna, forest, agricultural, and peat fires (1997–2009). Atmos. Chem. Phys. 10, 11707–11735. http://dx.doi.org/10.5194/acp-10-11707-2010.

van Donkelaar, A., Martin, R.V., Leaitch, W.R., MacDonald, A.M., Walker, T.W., Streets, D.G., Zhang, Q., Dunlea, E.J., Jimenez, J.L., Dibb, J.E., Huey, L.G., Weber, R., Andreae, M.O., 2008. Analysis of aircraft and satellite measurements from the Intercontinental Chemical Transport Experiment (INTEX-B) to quantify long-range transport of East Asian sulfur to Canada. Atmos. Chem. Phys. 8 (11), 2999–3014. http://dx.doi.org/10.5194/acp-8-2999-2008.

Vestreng, V., Klein, H., 2002. Emission Data Reported to UNECE/EMEP: Quality Assurance and Trend Analysis & Presentation of WebDab (MSC-W Status Report).

Wells, K.C., Millet, D.B., Cady-Pereira, K.E., Shephard, M.W., Henze, D.K., Bousserez, N., Apel, E.C., de Gouw, J., Warneke, C., Singh, H.B., 2014. Quantifying global terrestrial methanol emissions using observations from the TES satellite sensor. Atmos. Chem. Phys. 14 (5), 2555–2570. http://dx.doi.org/10.5194/acp-14-2555-2014-supplement.

Wesely, M.L., 1989. Parameterization of surface resistances to gaseous dry deposition in regional-scale numerical models. Atmos. Environ. 23 (6), 1293–1304. http://dx.doi.org/10.1016/0004-6981(89)90153-4.

White, J.C., Wagner, W.R., Beal, C.N. (Eds.), 1989. Global Climate Change Linkages: Acid Rain, Air Quality, and Stratospheric Ozone. Springer, ISBN 0-444-01515-9.

Worden, H.M., Deeter, M.N., Frankenberg, C., George, M., Nichitiu, F., Worden, J., Aben, I., Bowman, K.W., Clerbaux, C., Coheur, P.F., de Laat, A.T.J., Detweiler1, R., Drummond, J.R., Edwards, D.P., Gille, J.C., Hurtmans, D., Luo, M., Martínez-Alonso, S., Massie, S., Pfister, G., Warner, J.X., 2013. Decadal record of satellite carbon monoxide observations. Atmos. Chem. Phys. 13, 837–850. http://dx.doi.org/10.5194/acp-13-837-2013.

Yashiro, H., Sugawara, S., Sudo, K., Aoki, S., Nakazawa, T., 2009. Temporal and spatial variations of carbon monoxide over the western part of the Pacific Ocean. J. Geophys. Res. 114 (D8), D08305. http://dx.doi.org/10.1029/2008JD010876.

Yevich, R., Logan, J.A., 2003. An assessment of biofuel use and burning of agricultural waste in the developing world. Glob. Biogeochem. Cycles 17 (4). http://dx.doi.org/10.1029/2002GB001952.

Zhang, Q., Streets, D.G., Carmichael, G.R., He, K.B., Huo, H., Kannari, A., Klimont, Z., Park, I.S., Reddy, S., Fu, J.S., Chen, D., Duan, L., Lei, Y., Wang, L.T., Yao, Z.L., 2009. Asian emissions in 2006 for the NASA INTEX-B mission. Atmos. Chem. Phys. 9, 5131–5153. http://dx.doi.org/10.5194/acp-9-5131-2009.

Zhao, Y., Nielsen, C.P., Lei, Y., McElroy, M.B., Hao, J., 2011. Quantifying the uncertainties of a bottom-up emission inventory of anthropogenic atmospheric pollutants in china. Atmos. Chem. Phys. 11, 22952308. http://dx.doi.org/10.5194/acp-11-2295-2011.

Zhu, L., Henze, D.K., Cady-Pereira, K.E., Shephard, M.W., Luo, M., Pinder, R.W., Bash, J.O., Jeong, G.R., 2013. Constraining U.S. ammonia emissions using TES remote sensing observations and the GEOS-Chem adjoint model. J. Geophys. Res. 118 (8), 3355–3368. http://dx.doi.org/10.1002/jgrd.50166.